ICARUS 103, 235–252 (1993)

IRTF Observations of the Occultation of 28 Sgr by Saturn

JOSEPH HARRINGTON,*[,1,2] MAREN L. COOKE,* WILLIAM J. FORREST,‡[,2] JUDITH L. PIPHER,‡[,2]
EDWARD W. DUNHAM,*[,3] AND J. L. ELLIOT*[,†]

*Department of Earth, Atmospheric, and Planetary Sciences, Room 54-410, Massachusetts Institute of Technology, Cambridge, Massachusetts 02139; †Department of Physics, Massachusetts Institute of Technology, Cambridge, Massachusetts 02139; and ‡Department of Physics and Astronomy, University of Rochester, Rochester, New York 14627

Received November 4, 1992; revised March 24, 1993

We obtained an infrared-imaging time series (λ = 3.255 μm, Δt = 0.25 sec) of the 1989 July 3 occultation of 28 Sgr by Saturn and its rings using the NASA Infrared Telescope Facility (Mauna Kea, HI) and the University of Rochester 62 × 58-pixel InSb array camera. The radial extent of the beam in the ring plane was ~20 km, and the rings were sampled approximately every 5 km. The images show stellar signal throughout the ring event, including the densest parts of the B ring, although some signal may be due to indirect light diffracted into the beam (P. D. Nicholson, O. Perkovic, K. Matthews, and R. G. French 1991, *Bull. Am. Astron. Soc.* 23, 1178). The time associated with each pixel readout is accurate to within 60 μsec of UTC. We present a table of interpolated ring event times.

Although qualitative ring structure at scales of 10–100 km is consistent with the Voyager stellar and radio occultation profiles, our profile varies systematically with respect to the Voyager data over large radius scales. The most likely explanation for this is indirect stellar signal diffracted through the rings; to date there is no quantitative model of this effect, and the ring masses derived here have not been corrected for it.

The projected stellar diameter of ~20 km put most density- and bending-wave trains below our resolution; fitting models to these waves for surface mass density was therefore not attempted. The Voyager Photopolarimeter Subsystem occultation data do not suffer such smearing, so the mass extinction coefficient determined by L. W. Esposito, M. O'Callaghan, and R. A. West (1983, *Icarus* 56, 439–452) was used to estimate the mass of the rings, based on the 1989 July 3 data. The masses derived in this fashion are $(2.42 \pm 0.93) \times 10^{22}$ g (total), $(0.097 \pm 0.037) \times 10^{22}$ g (C ring), $(1.84 \pm 0.71) \times 10^{22}$ g (B ring), and $(0.49 \pm 0.19) \times 10^{22}$ g (Cassini division and A ring). We present masses and mean optical depths of individual ring sections.

INTRODUCTION

On 1989 July 3, Saturn, its rings, and Titan occulted 28 Sgr, a K4 giant star with magnitudes: K = 1.50 ± 0.04, I = 3.90 ± 0.06 (Neugebauer and Leighton 1969), and V = 5.388 ± 0.011 (Sinachopoulos 1989). Considering only photon statistics, this event had the highest signal-to-noise ratio of any occultation by Saturn observed since the advent of modern detectors, and it was the first occultation by Saturn's rings where stellar signal was detectable throughout the entire event. Taylor (1983) first predicted the occultation, and it was also discussed by Killian and Dalton (1985).

The star's sampling beam at Saturn's distance spans ~20 km, so features much smaller than 20 km are not readily discernible from this occultation. The angle between the beam and the ring plane was 25°24′14″, but fortunately the occultation path ran roughly in the direction of the minor axis of the projected beam ellipse (see Fig. 1). Although Sinachopoulos (1989) reports the star as double, the companion is located 12″.9 away and has a V magnitude of 13.5; we did not detect this star in the short exposures used during the occultation.

Most major telescopes in the viewing area recorded the event (Brahic *et al.* 1989, di Cicco and Robinson 1989, Dunham *et al.* 1989, French *et al.* 1989, Harrington *et al.* 1989, Hubbard *et al.* 1989, Porco *et al.* 1989, Reitsema *et al.* 1989, and Sicardy *et al.* 1989). Many observers worked in the infrared, both to maximize stellar signal and to minimize reflected light from the planet and rings. They chose absorption bands of molecular species in Saturn's atmosphere (CH_4) and (for those sites with sufficiently dry skies) rings (H_2O) to reduce reflected light still further.

Several observers used imaging detectors. These systems have the advantages that the photometric aperture can be placed on the image after the fact, substantially reducing noise introduced by tracking errors; the background light field can be fitted and removed far more accurately than is possible with single-channel photome-

[1] To whom correspondence should be addressed.

[2] Visiting Astronomer at the Infrared Telescope Facility, which is operated by the University of Hawaii under contract from the National Aeronautics and Space Administration.

[3] Present address: MS 245-6, NASA Ames Research Center, Moffett Field, California 94035

0019-1035/93 $5.00

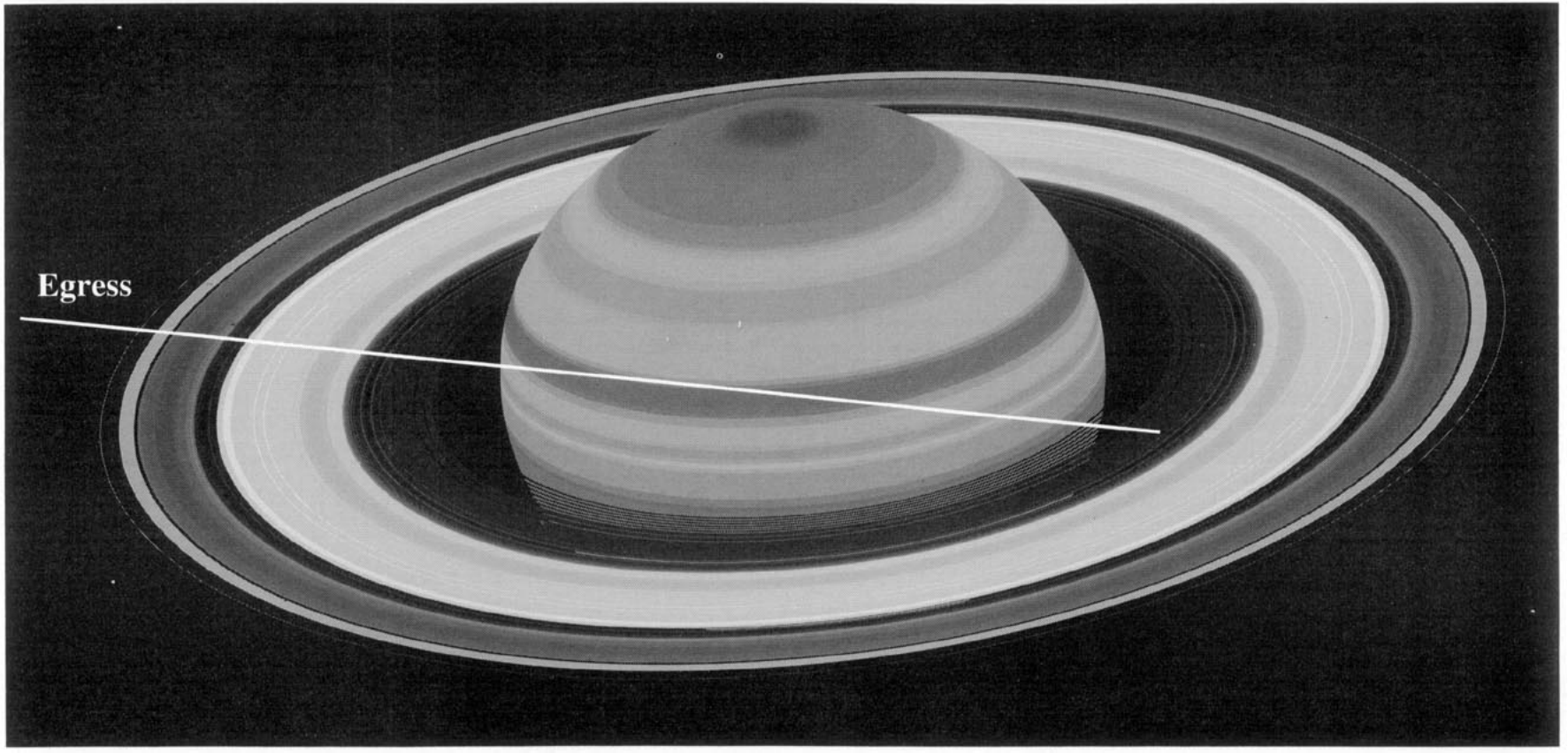

FIG. 1. Event geometry for the occultation as viewed from the IRTF. The white line is the path of the star as we recorded data.

ters, providing higher quality data and allowing observation of fainter stars; and the images themselves can be inspected if anomalies are found in the lightcurve or to identify events of spatial significance, such as the location of a central flash. However, imaging photometers generate copious quantities of data, making data storage and analysis more difficult. In addition, few of these systems are capable of operation at high speed or with accurate synchronization to an external time signal.

We present here our observations of the event with the NASA Infrared Telescope Facility (IRTF) and the University of Rochester IR array camera, our method for generating optical depth profiles, and our first ring results. These results include ring feature times, a discussion of ring profile morphology, and ring mass estimates. We discuss the challenges associated with imaging observations of occultations, and our approaches to them, in the appendix.

OBSERVATIONS

We obtained a time series of 44,408 infrared images of the 28 Sgr occultation with the University of Rochester 62 × 58-pixel InSb array camera (Forrest *et al.* 1989) at the IRTF on Mauna Kea, Hawaii. We achieved absolute timing by running the camera's computer directly from an accurate clock (see Timing System, below). Event and observational parameters are summarized in Table I.

TABLE I
1989 July 3 Occultation Parameters

Telescope	3.0-m NASA Infrared Telescope Facility
Site	Mauna Kea, Hawaii
Star	28 Sgr = SAO 187255, HD 173469, BD −22°4854, HR 7046
Spectral type	K4 III (Neugebauer and Leighton 1969)
V Magnitude	= 5.388 ± 0.011 (Sinachopoulos 1989)
K Magnitude	= 1.5 ± 0.04 (Neugebauer and Leighton 1969)
Sky-plane beam diameter	~20 km
Radial beam velocity	~20 km/sec
Beam-ring plane angle	25°24′14″
Camera	U. of Rochester 62 × 58-pixel InSb array
Stored frame size	62 × 12 pixels
Pixel scale	0.″42/pixel
λ_0	= 3.255 μm (methane and water ice absorption)
$\Delta\lambda$	= 0.230 μm
Exposure time	0.25 sec (3 averaged $\frac{1}{12}$ sec exps)
Timing system accuracy	±60 μsec per pixel, ±1 msec per frame, absolute
Data start	6:46:00 UTC (C ring during ingress)
Data end	9:51:00 UTC (well outside F ring)

The filter wavelength is in a water ice absorption band and inside the edge of a methane absorption band (see Table I). This minimized background light from the rings and planet, respectively, simplifying image processing. We were fortunate to have had a clear night, with occasional patchy cirrus clouds on the horizon but none seen overhead; the hygrometer read 0% relative humidity as we started taking data. Despite careful monitoring of temperature, the signal level of the star in unocculted regions rose smoothly in time throughout the event. We believe that a small amount of moisture may have condensed on the dewar window prior to the occultation and slowly evaporated. We corrected for this effect in the analysis.

The unocculted star was bright enough to saturate the detector in less than $\frac{1}{4}$ sec. In addition, data storage capacity was limited to 80 Mbytes, due to constraints in the camera computer. To reduce the quantity of data to a manageable amount, avoid image saturation, and still comfortably oversample the lightcurve as smoothed by the star's projected diameter, we recorded just 12 rows (rows 6–17, chosen for their cosmetic quality), exposed for $\frac{1}{12}$ sec, and averaged three successive exposures to generate each recorded image.

One of the diagonal mirrors in the camera was apparently damaged in shipment and had to be replaced by a slightly smaller one. The 12 lowest-numbered columns were thus vignetted, causing this region to lose celestial signal and to be illuminated by thermal radiation from the diagonal mirror's support structure. Background and flat frame correction did not completely remove these effects, so we ignored these columns in the analysis. Unfortunately, the star reappeared from planet occultation in this area, so we have been unable to produce a reliable atmospheric emersion lightcurve.

Because of problems with the telescope control system, we acquired Saturn well into ring ingress. We took several full-frame bias, flat-field, sky, and planet images before and after the event (see Data Reduction, below). Data recording began at 6:46:00 UTC and ran continuously until 9:51:00 UTC. We nodded the telescope south 9″ at 7:46:24 and back to the base position at 8:00:00, but did not observe a central flash.

TIMING SYSTEM

Occultation work requires precise timing; our ~20-km/sec projected stellar velocity would produce a detectable 1-km shift in sharp ring-edge features if the timing were to drift by just 0.05 sec. Further, if a dataset is included in an astrometric solution involving more than one observation, accurate synchronization to a common time base is necessary to eliminate an unknown time shift as a degree of freedom per observatory in the fit (French *et al.* 1993).

Our timing system used a portable quartz occultation clock (Baron 1989) to drive the camera's computer directly. This clock has a frequency accuracy of approximately 10^{-9} (maximum drift over time Δt of 10^{-9} Δt). There were two independent checks in the system: the IRTF's Geostationary Operational Environmental Satellites (GOES) receiver and a portable rubidium standard borrowed from the National Institute of Standards and Technology's WWVH station at Barking Sands, Kauai, Hawaii. These three time sources are hereafter referred to as the MIT clock, the GOES receiver, and the Rb clock, respectively. The GOES receiver is a Kinemetrics Model 468-DC GOES Satellite Synchronized Clock, nominally accurate to within 1 msec of UTC, though satellite motions are not taken into account. The Rb clock's nominal accuracy is 10^{-12}.

On 1989 July 1 at 00:07 UTC, the Rb clock's frequency was adjusted to match that of the primary time standard at WWVH and brought to Mauna Kea (the Rb clock was also synchronized to the primary, but lost synchronization on the way to Mauna Kea). The MIT clock's frequency was tuned to match the Rb clock's and it was synchronized to the GOES receiver for an approximation of the correct time. The MIT clock fed a 20-Hz signal to a phase-locked loop (PLL) circuit which generated a 60-Hz signal. This 60-Hz signal was passed to the bus interrupt line of the Rochester camera's computer.

Computers synchronize data transfers between their various components with bus interrupt signals; in the case of the Rochester camera's computer these occur 60 times each second. Interrupt service routines (ISRs) in the computer's real-time operating system run immediately upon receipt of an interrupt and generate a request-for-data (RFD) signal on the bus. The RFD is sensed by the infrared array and triggers a frame readout/clear operation if one is scheduled. The readout/clear operation sequentially resets each pair of pixels by reading their accumulated charge through a pair of amplifiers. Since there is no shutter, the chip is sensitive to light even as it is being read. This essentially eliminates dead time between integrations, but causes the beginning and end of an integration interval to vary across the detector (the duration of integration remains constant). For this dataset, the time associated with each frame is the mid-time of integration at the location of the center of the stellar image.

The time of each pixel readout relative to the MIT clock is thus known to an accuracy dependent upon the variation in the lengths of ISRs and upon the stability of the PLL. Together these uncertainties are less than 60 μsec, and since they dominate the uncertainty and drift due to the MIT clock, absolute timing accuracy for any given pixel is also 60 μsec. Each pixel pair takes 36 μsec to read out, so the read time per row is 1.116 msec. The star's position was constant to within ± 1 pixel, and we did not compensate for stellar image motion in the timing solution, so the time associated with each frame is within $\sim$1 msec of UTC.

During the event, we used the offset counter in the MIT clock to measure the differences between all time sources with a resolution of 200 nsec. We also watched diagnostic 1-Hz signals from all sources on an oscilloscope, and ran a strip chart which recorded the 1-Hz signal from the MIT clock and the exclusive-OR of this signal and a 1-Hz signal generated by the computer. During the event, the total drift between the MIT and Rb clocks was 200 nsec. The GOES receiver drifted 694.4 μsec between 4:45:00 and 9:56:00 UTC, which the WWV office in Boulder, Colorado, has attributed to satellite motions.

The PLL lost lock 42 times during the event, oscillating in frequency for a few seconds until it regained its lock. In each of these events, three extra interrupts occurred (in one case, two extra interrupts occurred). The oscillation left an obvious signature in the data, and the additional interrupts caused the waveform recorded on the strip chart to change. In the analysis, we identified each event and corrected for the resultant discrete timing error. Up to 35 images after each event were marked as "bad" to eliminate the possibility of residual effects contaminating the analysis (these are the small gaps in Fig. 3, for example at 85,000 km).

We returned the Rb clock to the WWVH station, where the staff measured its offset and frequency relative to the primary time standard on 1989 July 3 at 23:30 UTC. This offset agreed with the offset relative to the GOES receiver during the event to within the GOES receiver's accuracy. The WWVH staff found the Rb clock's time to be drifting less than 100 nsec/day. Our timing calculations used the Rb clock's offsets relative to the primary and the MIT clock, rather than the GOES receiver's offset relative to the MIT clock, because the GOES receiver is inherently much less accurate.

Since the MIT clock ran the computer directly, each frame readout represents a timing signal from a calibrated, stable time source placed directly into the data. This electronic, directly causal means of associating times with data frames avoids the timing uncertainties inherent in mechanical means such as chopping with the secondary mirror, and obviates the need to model the behavior of a computer's clock with respect to an accurate one when associating times with data points.

DATA REDUCTION

Several corrections must be made to an astronomical array image before the numerical value of each pixel is proportional to the intensity of light from the correspond-

ing area of the sky. These corrections eliminate the most pronounced electronic and atmospheric effects. Bias is the electronic "zero" of the array's readout amplifier, and must be subtracted from each pixel value so that zero in the data corresponds to zero light level. Pixel-to-pixel variations in sensitivity are removed from the image by dividing by a normalized flat field frame, which is an image of a uniformly lit source. These and other basic corrections are described in more detail elsewhere (e.g., Conner 1984). In the infrared, the thermal emission of the sky is often subtracted, and for bright subjects there is usually a correction for nonlinear chip response to differing light levels.

For ease of handling, the data were broken into six sequential computer files of occultation images, plus individual error-correction frames taken before and after the event. Bias frames were consistent before and after the event, so we averaged them to generate the frame used to process the images. The sky frames varied significantly between the pre- and post-occultation sets, so the members of each set were averaged to produce a representative frame. We then generated six new sky frames by interpolating each pixel to the mid-time of each of the six data files. The flat field was made from images of the unfocused inside of the observatory dome and similar images of the sky to eliminate thermal contributions from the telescope itself.

The Santa Barbara Research Center 62 × 58-pixel InSb array chips are known to have a nonlinear response to light. This effect is primarily caused by the increase in capacitance of each photodiode as the back bias decreases during an exposure (Forrest *et al.* 1990). The linearization function appropriate to this dataset is given by

$$\mathrm{lin}(A) = Ae^{A/192{,}000}, \tag{1}$$

where A is measured signal in analog-to-digital conversion units (ADU) and $\mathrm{lin}(A)$ is linearized signal. One ADU corresponds to approximately 60 electrons. The functional form above was calibrated empirically by observing the signal from a flat-field source of constant flux f with varying integration times Δt. The logarithmic derivative for all pixels was fit adequately over a range of A easily containing the extremes in our data by

$$\frac{d\ \ln(f\Delta t)}{d\ \ln(A)} = 1 + mA, \tag{2}$$

which integrates to the linearization function.

The total image correction is

$$F = \mathrm{lin}(F_{\mathrm{dome}} - B) - \mathrm{lin}(F_{\mathrm{sky}} - B), \tag{3}$$

$$C = \frac{\langle F\rangle}{F}\,(\mathrm{lin}(R - B) - \mathrm{lin}(S - B)), \tag{4}$$

where F is a pixel value in the corrected flat-field image, F_{dome}, F_{sky}, and B are the corresponding pixels in the averaged dome flat, sky flat, and bias images, respectively, C is a pixel value in the corrected image, R and S are the corresponding pixels in the raw data and interpolated sky images, respectively, and $\langle F\rangle$ is the mean pixel value of the flat field.

To determine the star signal above the ring background, we used the Aperture Photometry Package (Davis 1987) of the Image Reduction and Analysis Facility (IRAF) (Tody 1986). This software measures signal falling on an arbitrary aperture centered on the star (the "raw" region) and on a surrounding "background" region. In our case, the background region includes light from the sky as well as some light from the ring and planet. The raw region contains light from the star in addition to these sources; subtracting the area-weighted background signal from the raw signal gave the "star" value for each frame.

We used two different arrangements of apertures (see Fig. 2). For most of the images, the raw region was oblong, 14 pixels wide and 12 high with semicircular ends; the background region was a circle of 10 pixels' radius, truncated at the edges of the frame and excluding the raw region. The oblong shape was chosen to compensate for small tracking errors in the long dimension of the recorded image. We took advantage of the star's relative faintness in the optically thick B ring and our good fortune in guiding during this segment of the occultation and used a smaller, circular raw aperture for images in the B ring. This aperture, 5 pixels in radius, was immediately surrounded by a background annulus 8 pixels in radius and truncated at the edges of the image. The photometry regions used outside of the B ring were defined by polygons which were evaluated every 0.5 pixels (0".21); the circular B-ring apertures use the correct proportion of each pixel which intersects a circular border. Because of the tight tolerances of the image width, the polygonal apertures had a constant center in each data file, and the B-ring aperture centers were constant through the ring. The resulting lightcurve does not show the shifts in star values at borders of adjacent data files that would correspond to the abrupt shift from one sky frame to the next. This is an indication that the per-frame background subtraction was effective.

The signal level of the unocculted star increased fairly smoothly throughout the event, as mentioned under Observations. A linear function of time fit considerably better than an atmospheric extinction curve. We thus fit a line to signal levels in three unocculted regions, each an average of 201 consecutive star values. These values

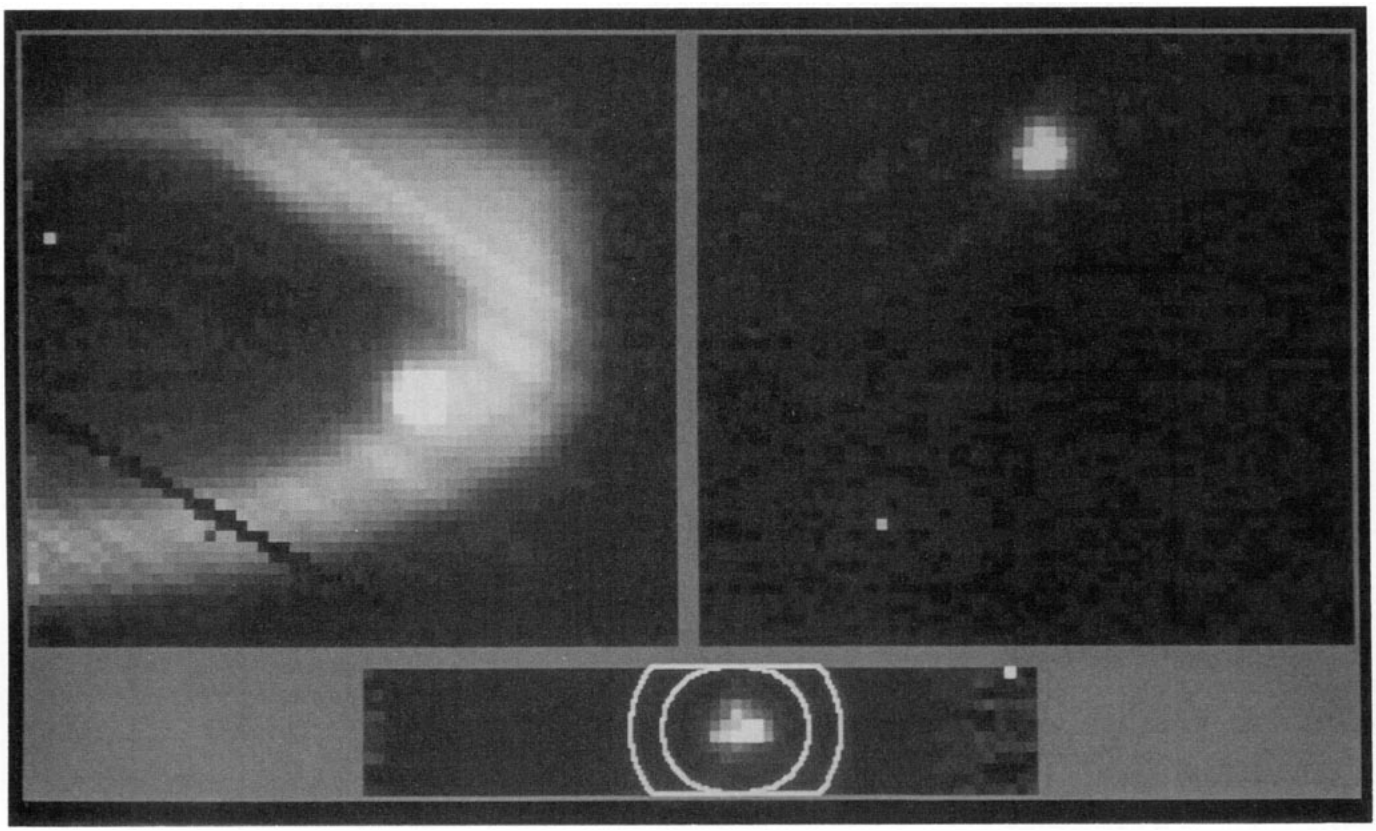

FIG. 2. The upper left image shows Saturn, the rings, and 28 Sgr viewed through a K filter just prior to the beginning of the occultation. The planet appears very dark because of absorption by atmospheric methane at this wavelength. The image in the upper right shows the scene in our occultation filter ($\lambda = 3.255$ μm, $\Delta\lambda = 0.230$ μm), with the star on the region of the chip (rows 6–17 from the top of the image) recorded during the event. Absorption by water ice in the rings as well as by atmospheric methane reduces the reflected sunlight to a very faint background. In both images, the background away from Saturn is approximately the same. The peak pixel values of the star are 12,365 ADU at K and 17,843 ADU in the occultation filter. These images are shown with the same linear brightness scale. The bottom image shows the first frame of the recorded occultation data, marked with the polygonal photometry apertures used in the A and C rings. The inner region is wider than it is high to deal with small tracking errors which occurred in the long dimension of the array (E–W). Within each file of images (total of six files), the center of the aperture is the same. We used a five-pixel circular aperture in the B ring to take advantage of better tracking and the fainter star. The three pixels in the upper right corner are the encoded time and array temperature, present in each occultation image, which provided a useful diagnostic during the analysis.

were taken from the clear region between the planet and the rings (both ingress and egress) and from a region well outside the F ring after egress. In all three cases we were careful to avoid the flux enhancement near the rings (see Optical Depth Profile Morphology, below). We calculated normal optical depths according to the formula

$$\tau_n = -\ln\left(\frac{I}{I_0}\right) \sin(\theta) \tag{5}$$

where τ_n is normal optical depth, I is stellar intensity, I_0 is unocculted stellar intensity (obtained from the linear fit to this value in clear regions during the occultation), and θ is the beam incidence angle of 25°24′14″ on the ring plane. The standard deviation of I/I_0 (0.25-sec integrations) in the three regions used to fit the I_0 line was 1.7, 1.5, and 1.0% of the transmission, respectively.

Finally, we tagged the lightcurve with ring-plane radii consistent to within a few kilometers of the Voyager radii for presumed-circular features. These radii assume the pole of Nicholson *et al.* (1990) and an offset for Saturn's position from the Jet Propulsion Laboratory DE-125 ephemeris of 1655 km east and 438 km south in the sky plane. Figure 3a, in the section on Optical Depth Profile Morphology, presents the resulting profile for the rings.

RING EVENT TIMES

In order to measure ring feature times, we interpolated the stellar signal between the 0.25-sec samples of the lightcurve. Event times are presented in Table II, along with estimated measurement uncertainties that depend both on the strength of the feature and on the relative noise level in the region. Typical measurement uncertain-

TABLE II
Ring Event Times

Feature number[a]	UTC	Error[b] (sec)	Comment[c]
36	06:47:08.589	0.10	core
37	06:49:14.089	0.03	
38	06:49:16.064	0.03	
43	06:50:15.002	0.02	Titan Gap o.e.
62	06:50:17.214	0.02	Titan ringlet o.e.
63	06:50:18.227	0.03	Titan ringlet i.e.
39	06:50:49.002	0.04	Plateau o.e.
40	06:51:29.664	0.04	Plateau o.e.
44	06:52:50.152	0.04	Innermost C ring
44	08:41:51.187	0.04	Innermost C ring
40	08:43:11.247	0.02	Plateau o.e.
39	08:43:51.857	0.03	Plateau o.e.
63	08:44:24.127	0.01	Titan ringlet i.e.
62	08:44:25.564	0.01	Titan ringlet o.e.
43	08:44:26.352	0.03	Titan Gap o.e.
38	08:45:24.517	0.03	
37	08:45:26.502	0.02	
36	08:47:31.484	0.05	core
35	08:49:33.364	0.02	Plateau i.e.
34	08:49:42.339	0.05	Plateau o.e.
33	08:50:14.314	0.02	
42	08:50:18.744	0.02	
31	08:50:26.129	0.05	
30	08:50:46.277	0.01	Plateau i.e.
29	08:50:56.627	0.02	Plateau o.e.
61	08:51:36.052	0.02	Maxwell ringlet i.e.
60	08:51:37.977	0.02	Maxwell ringlet o.e.
28	08:52:26.244	0.03	Plateau o.e.
59	08:52:31.054	0.03	1.47 R_S ringlet i.e.
58	08:52:31.856	0.02	1.47 R_S ringlet o.e.
27	08:52:52.899	0.02	Plateau i.e.
41	08:52:57.674	0.03	Plateau o.e.
26	08:53:19.786	0.03	Plateau i.e.
25	08:53:26.656	0.03	Plateau o.e.
57	08:53:35.556	0.03	1.495 R_S ringlet i.e.
56	08:53:38.294	0.01	1.495 R_S ringlet o.e.
24	08:53:47.531	0.02	Plateau i.e.
23	08:53:57.004	0.02	Plateau o.e.
22	08:54:58.706	0.05	B ring i.e.
83	08:56:48.744	0.04	B flat i.e.
82	08:57:30.369	0.05	B flat o.e.
81	08:58:38.889	0.05	B flatlet i.e.
80	08:58:53.031	0.05	B flatlet o.e.
79	08:59:10.331	0.08	B flux peak core
78	08:59:40.906	0.06	B flux peak i.e.
77	09:00:59.231	0.06	B drop
76	09:01:43.181	0.06	B flux peak i.e.
75	09:02:07.481	0.05	B broad flux peak i.e.
74	09:02:16.831	0.08	B broad flux peak o.e.
73	09:03:13.131	0.05	B flux peak i.e.
72	09:03:42.006	0.03	B flux peak i.e.
71	09:04:01.294	0.04	B flux peak o.e.
55	09:14:03.499	0.02	B ring o.e., Huygens Gap i.e.
54	09:14:16.269	0.02	Huygens ringlet i.e.
53	09:14:17.226	0.02	Huygens ringlet o.e.
20	09:14:21.226	0.02	Huygens Gap o.e.
19	09:14:32.414	0.02	1.96 R_S gap i.e.
18	09:14:34.729	0.03	1.96 R_S ringlet i.e.
17	09:14:35.894	0.03	1.96 R_S ringlet o.e.
16	09:14:36.881	0.03	1.96 R_S gap o.e.
13	09:14:52.344	0.02	
15	09:15:07.461	0.03	
14	09:15:55.189	0.01	1.990 R_S ringlet i.e.
12	09:15:56.944	0.02	1.990 R_S ringlet o.e.
11	09:16:04.749	0.03	
10	09:16:07.304	0.02	1.994 R_S gap i.e.
09	09:16:07.956	0.03	1.994 R_S gap o.e.
07	09:17:25.331	0.05	A ring i.e.
04	09:25:53.806	0.01	Encke Gap i.e.
03	09:26:08.119	0.01	Encke Gap o.e.
02	09:28:10.719	0.02	Keeler Gap i.e.
01	09:28:12.254	0.02	Keeler Gap o.e.
52	09:28:23.276	0.02	A ring edge
51	09:31:01.946	0.05	F ring core

[a] Feature numbers and precise locations are as reported in Nicholson *et al.* (1990) and modified by French *et al.* (1993); these numbers should not be used without reference to those works.

[b] Conservative, by-eye estimate of 2σ error.

[c] i.e., inner edge; o.e., outer edge; core, apparent center. Edges are located at the half-light level.

ties are 0.01–0.05 sec—generally within a few tenths of a sample. The larger uncertainties accompany features found in optically thick regions, where the transmitted stellar signal is more noisy. Regions having more complex optical depth profiles are also more difficult to measure, as closely-spaced variations limit the interval over which mean signal levels can be characterized.

This set of features is generally inclusive of those used for the pole solution of Nicholson *et al.* (1990) and is more fully described by French *et al.* (1993). Some features that had been assumed circular during earlier work have been found to be noncircular (or ambiguous) during the French *et al.* orbit fits; Table II uses the new designations. Some regions of the B ring that were obscured by high slant optical depths in the Voyager occultation data now permit reliable feature identification. These are included as features 71–83 both here and in French *et al.* (1993). Three members of this expanded set are the cores of narrow features and the times given represent their apparent centers, whether a signal peak (feature 51, the irregular F ring, and feature 79, newly identified in the inner B ring) or a minimum (feature 36, in the middle C ring).

The remainder of the features are the sharp edges of gaps, ringlets, or plateaux, and other abrupt optical depth transitions within the rings. These intrinsically sharp edges are smeared, however, by convolution with the large (~20 km) stellar diameter and appear as gradual ramps that are often further contaminated by noise. The

event times in Table II are the "half-light" times, measured by finding the point halfway between the mean signal on either side of the ramp and linearly interpolating between individual frame exposure times. This method can be uniformly applied to all edges in the sample, despite differences in noise level and surrounding ring characteristics. It is not ideal, since many of the edges are quite sharp and the diffracted intensity at the edge is $\frac{1}{4}$ the unocculted flux, rather than $\frac{1}{2}$. However, 28 Sgr is far from a point source, and as French *et al.* (1993) demonstrate, systematic radius errors for these measurements will be less than 0.1 km.

Our measurements of the features currently presumed circular are incorporated along with Voyager data and other 28 Sgr observations in the new geometry analyses that are presented by French *et al.* (1993) and Hubbard *et al.* (1993).

OPTICAL DEPTH PROFILE MORPHOLOGY

Figure 3a presents the IRTF egress ring optical depth profile. No attempt has been made to account for extinction efficiency effects due to wavelength or viewing geometry (see below). The small section of C ring data available from ingress is essentially identical to the egress data presented here. There are two major qualitative differences between the infrared profiles from this event and the Voyager data. The first effect is a smearing of fine detail in our data; the second is a systematic variation in optical depth over large radius scales.

Spatial resolution was limited by the projected stellar diameter of ~20 km. Most of the numerous density- and bending-wave trains, which were the focus of much of the post-Voyager analysis effort, are unfortunately below this resolution; Fig. 4 shows three profiles of the Mimas 5 : 3 density wave. Figure 4a is the original Voyager Photopolarimeter Subsystem (PPS) profile (Esposito *et al.* 1983a), at a resolution of 0.5 km. Figure 4b is the PPS profile at 20-km resolution, showing the loss of all but the first few peaks. The last profile shows the IRTF 28 Sgr data, with even fewer resolved peaks. Likely the most useful wave information to be gained from this dataset will involve determining the phases of those waves whose leading undulations survived the convolution. Both calibrated PPS datasets used in this section were provided by the Rings Node of the Planetary Data System.

On scales slightly larger than this smearing effect, the general qualitative appearances of the profiles match very well, except for the expected differences in location of noncircular features and for the differing phases of the visible portions of density and bending waves. Superposing the profiles as in Fig. 3c shows that edges line up very well and that the general shapes and widths of ramps and ringlets are similar between the two profiles. The structure of the rings on these scales appears not to have undergone major qualitative changes in the nearly 9 years between the first Voyager flyby and the 28 Sgr occultation.

When the 20-km PPS and IRTF 28 Sgr profiles are subtracted, as in Fig. 3d, systematic differences between the PPS and 28 Sgr profiles become more evident. These differences are primarily on scales much larger than those considered above. A fairly regular offset of the two profiles appears in the C ring and a slope is seen in the A ring. In some regions, notably in the B ring adjacent to its edges, the optical depth is reduced considerably compared with the Voyager profile. The most opaque region in the ring, 104,000–110,000 km from Saturn's center, seems "smoothed over," but the images show signal above the ring background. Immediately outside the ring, the unocculted stellar signal rises by ~0.2 optical depths to meet the ring. Nicholson *et al.* (1991) have tentatively associated these effects with indirect light diffracted through the rings and the extinction efficiency of ring particles at infrared wavelengths: the ring particles diffract light with a distribution function that decreases with increasing deflection angle. This produces a faint halo around the bright stellar image. Since the photometry aperture (whose size is determined by the seeing) projects onto a moderately large region of the ring, the integrated light from this halo is enough to affect the profile qualitatively in the densest and clearest areas.

Outside the F ring at 143,141 km from Saturn's center, a single data frame has an anomalously high optical depth ($\tau_n = 0.06$, transmission = 0.87 of full flux) for the region (see Fig. 5). The immediately surrounding profile has a full flux of 1.001 ± 0.013, making this a 10σ feature. The

FIG. 3. IRTF egress and Voyager PPS ring occultation optical depth profiles. (a) IRTF 28 Sgr profile. Small structure at 143,000 km is real but could not be a ringlet (see text). No attempt has been made to adjust the optical depths for wavelength-dependent differences in extinction efficiency. (b) PPS profile averaged in flux to 20-km resolution. (c) Superposed IRTF 28 Sgr and PPS 20-km profiles. Detailed features line up well. However, a large-scale difference in optical depths is apparent. In most regions the IRTF data has lower optical depth and is smoother. (d) Difference between IRTF 28 Sgr and PPS 20-km profiles. Large-scale differences are now very apparent, including several regions (e.g., 100,500, 116,000, and 123,000 km) of suppressed optical depth and a ramp from 122,000 km through the outer edge of the A ring. Although the issue is far from resolved, a likely explanation for some of the effects may be indirect signal diffracted into the beam from particles nearby (Nicholson *et al.* 1991). Note noncircular features at, e.g., 77,800 and 140,000 km. Gaps in IRTF profile are due to timing circuit instabilities. Downward spike in PPS profile at 126,700 km has been attributed to instrument error. Axis scales vary as appropriate to each ring. Voyager data courtesy PDS Ring Node.

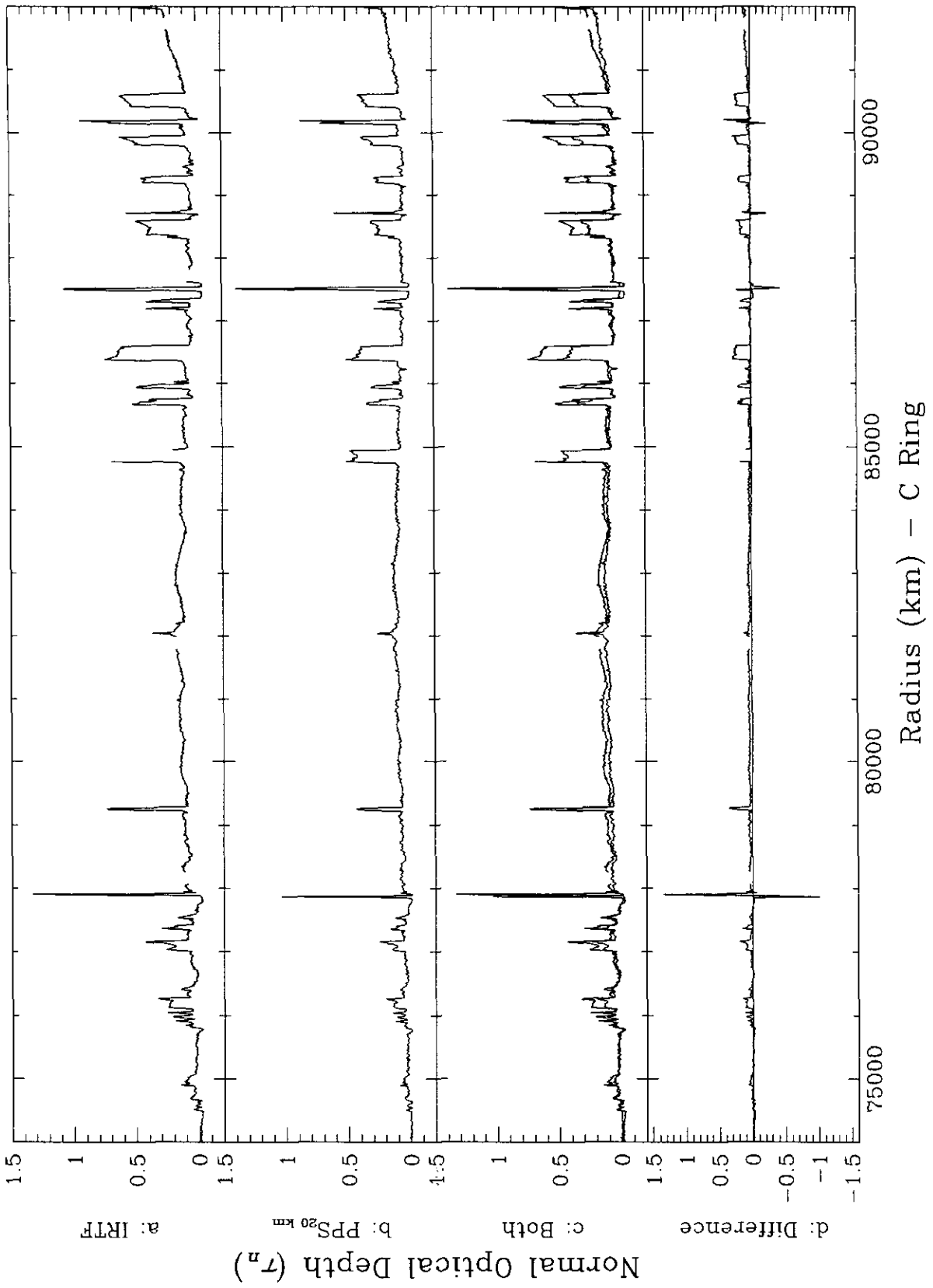
Normal Optical Depth (τ_n)
a: IRTF
b: PPS$_{20\ km}$
c: Both
d: Difference
1.5
1
0.5
0
−0.5
−1
−1.5
75000
80000
85000
90000
Radius (km) − C Ring

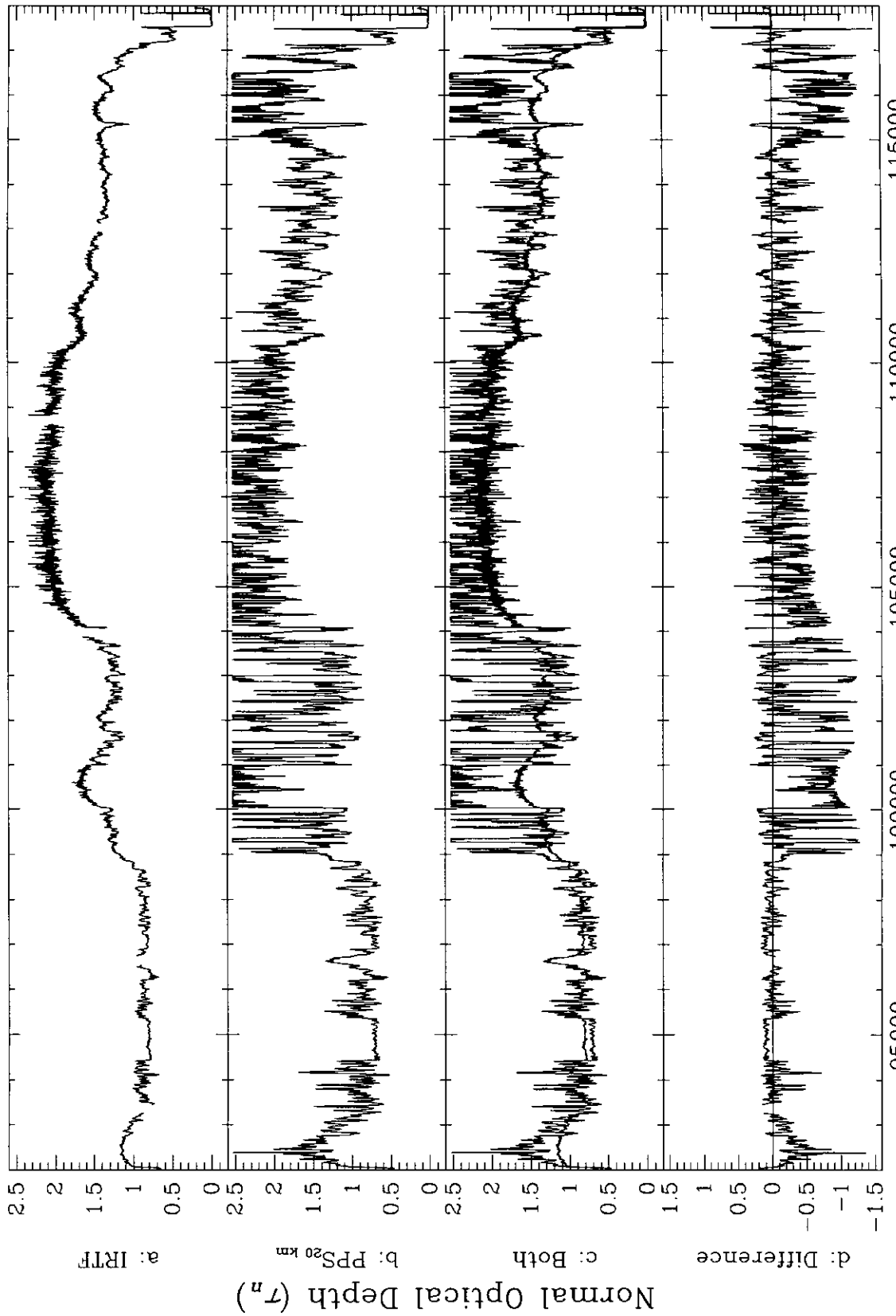

FIG. 3—*Continued*

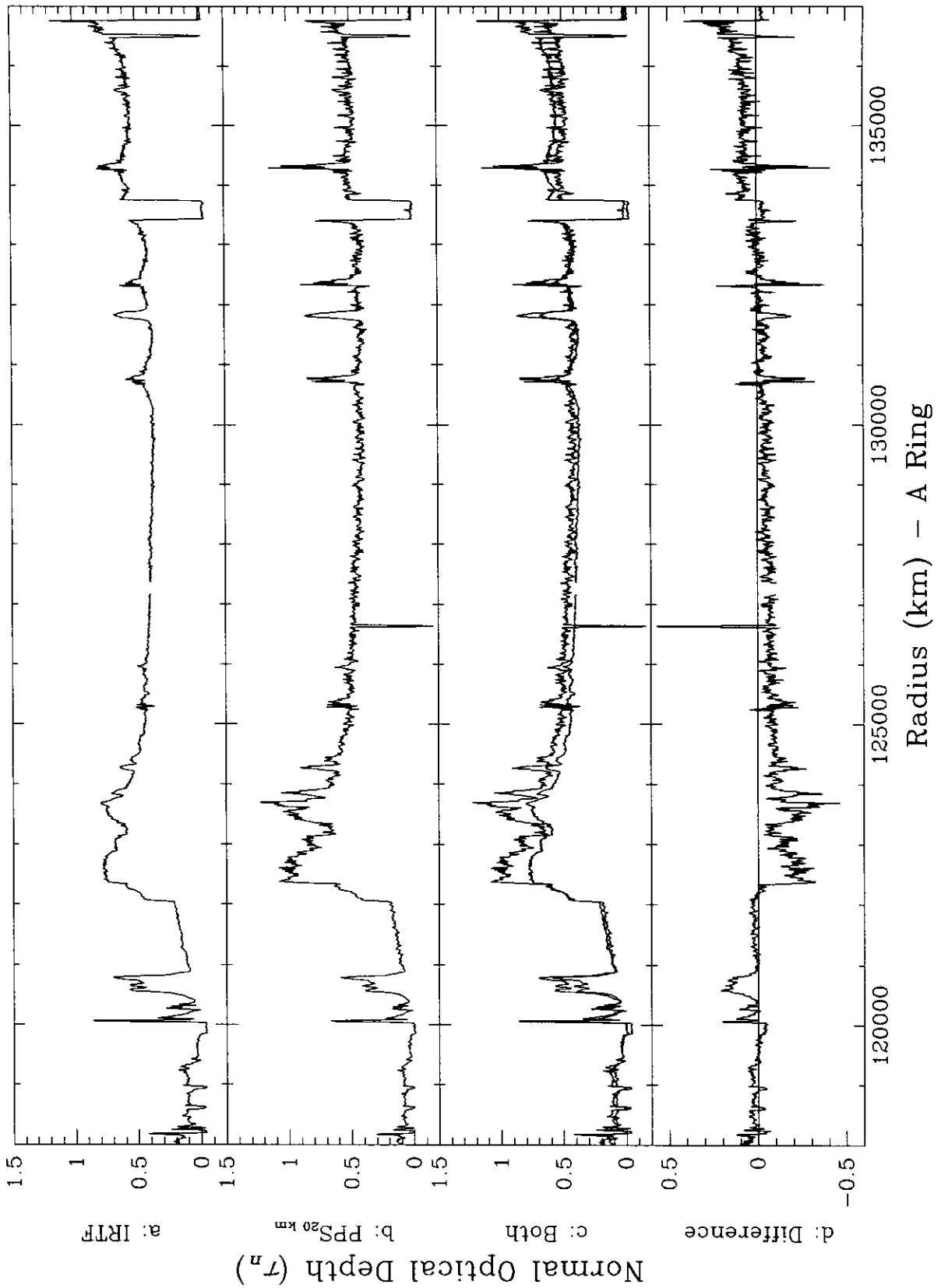

FIG. 3—*Continued*

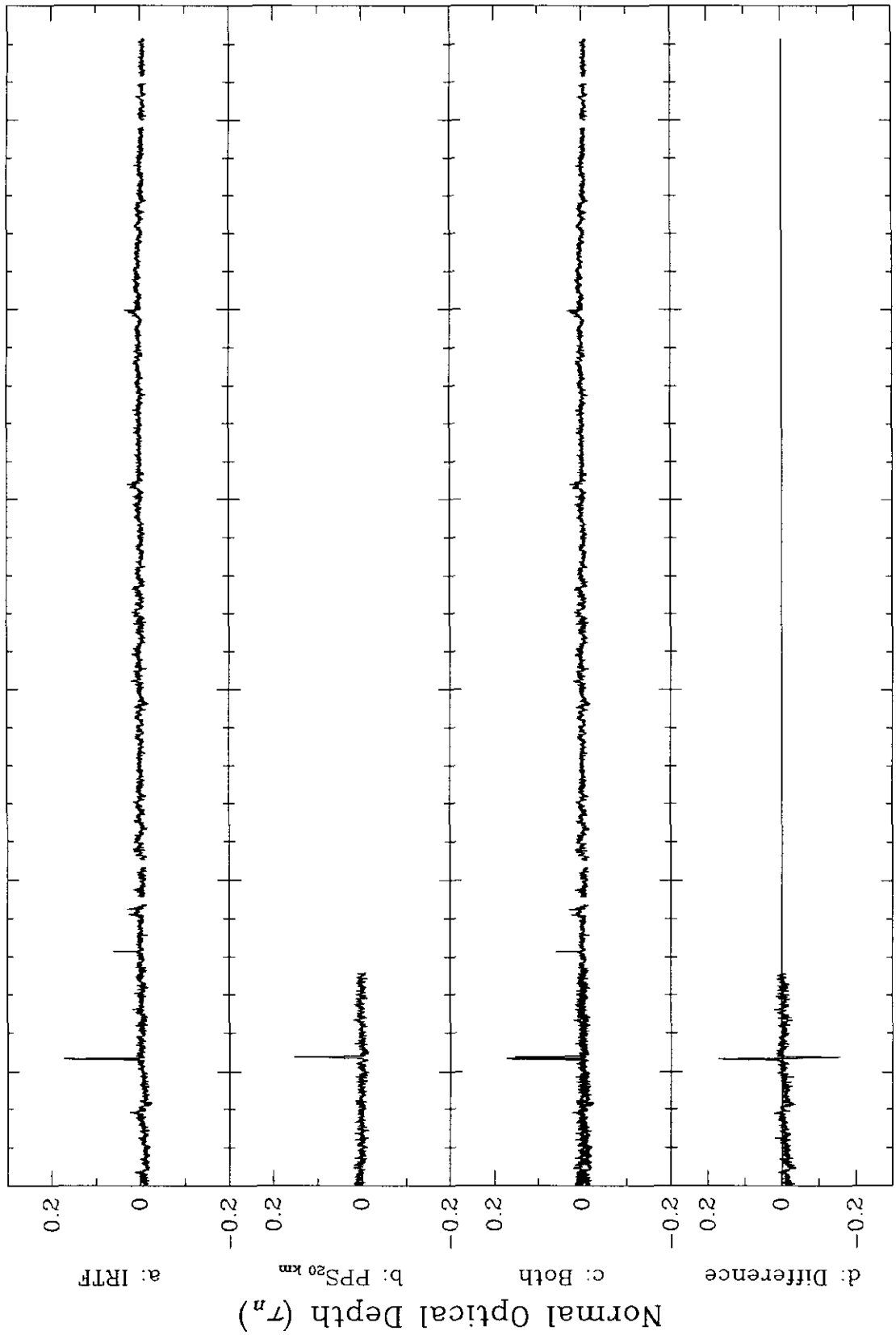

FIG. 3—*Continued*

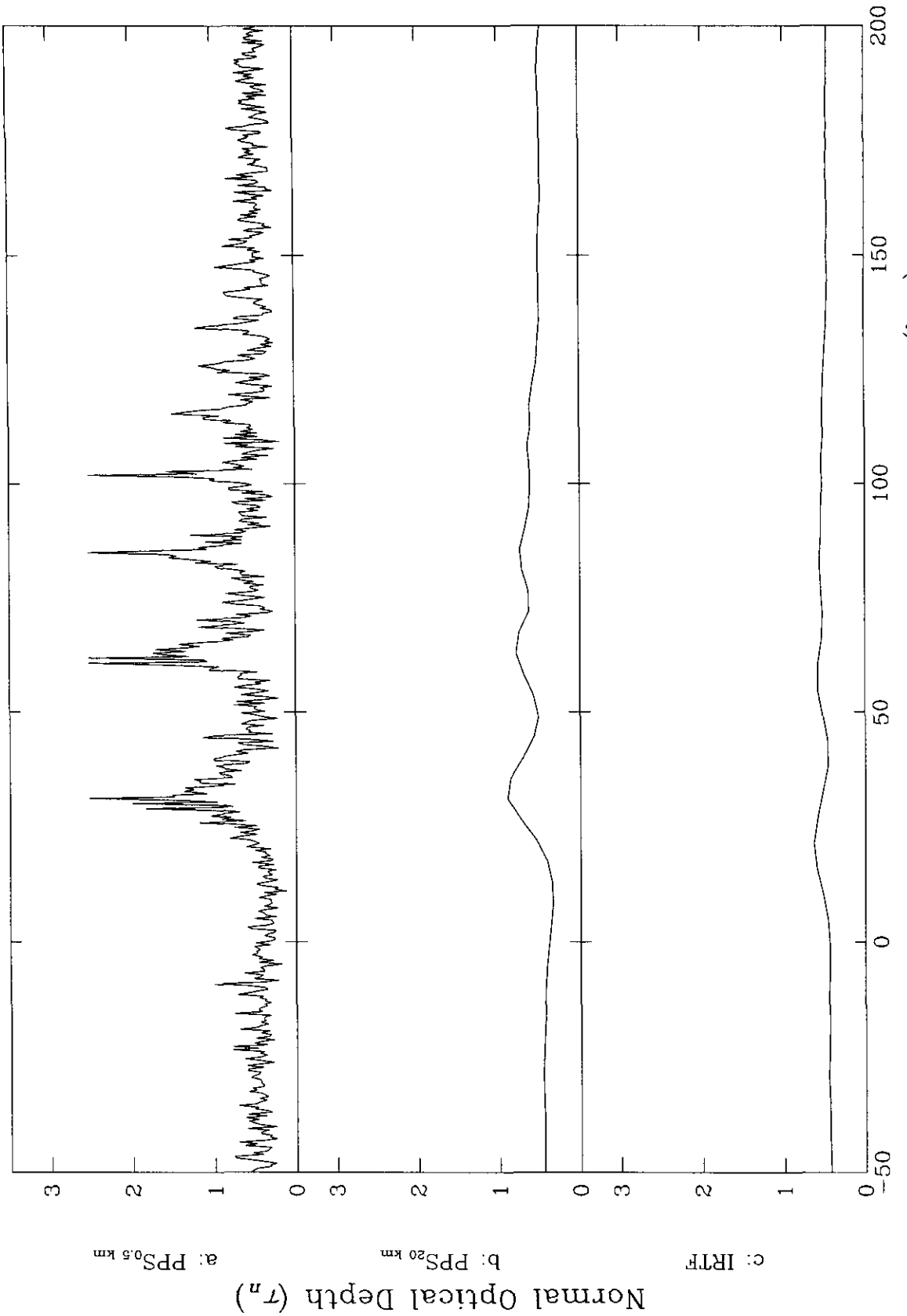

FIG. 4. Most ring structures narrower than the ~20-km projected stellar diameter were not visible in this event because of convolution with the occultation beam; this included almost all density- and bending-wave trains. Shown here are (a) the Mimas 5:3 density wave in a familiar 0.5-km-resolution version of the Voyager PPS optical depth profile, (b) the same feature in a version of the PPS profile averaged in flux over 20 km, and (c) the feature in the IRTF 28 Sgr occultation data. Voyager data courtesy PDS Ring Node.

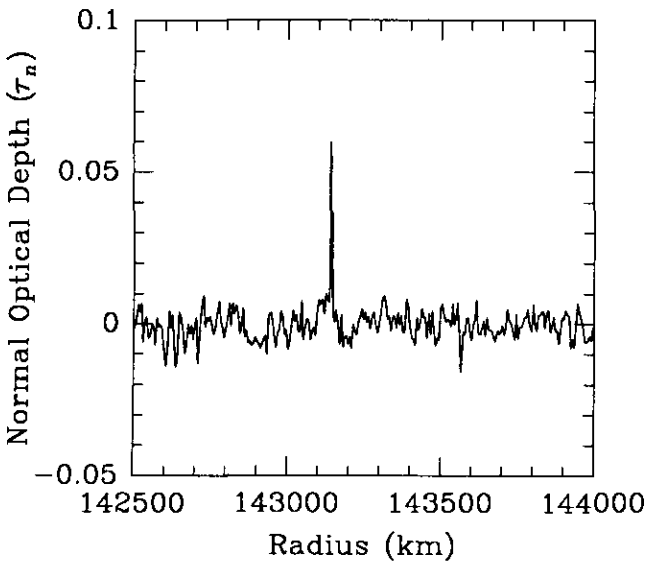

FIG. 5. This new feature, located exterior to the F ring at 143,141 km from Saturn's center, occurs in a single image, which is normal in all respects. The sampling rate was such that a ringlet would appear on several consecutive frames, ruling out the possibility that the feature is an undiscovered ringlet. Further possibilities are discussed in the text.

image associated with this point is normal in all respects. Nowhere else in the data stream does such an anomalous feature appear. We believe the feature is probably real in the sense that it was not due to equipment failure or clouds. However, given its singular nature all we can say for certain is that it is not a ringlet, since our 4× oversampling would cause a ringlet to appear on several consecutive frames. If the event is indeed an occultation by a stray member of the putative F-ring moonlet belt (Cuzzi and Burns 1988), the moonlet would need to block 13% of the beam. If the beam is 20 km in diameter, the corresponding spherical body's diameter would be 7.2 km, which is within the range of 0.1–10 km proposed by Cuzzi and Burns.

RING MASSES

Prior to the Voyager encounter, the mass of Saturn's rings was undetermined. Imaging and other direct observations did little to indicate what the mass could be, and the rings did not observably affect the orbits of the moons or the trajectory of Pioneer 11. Null *et al.* (1981) calculated an upper bound of 1.7×10^{-6} Saturn masses (9.7×10^{23} g) from this latter fact.

However, optical depth is directly related to the total mass of material in the beam. If one makes several assumptions about ring composition and uses models to fit for the surface mass density at many locations, one can use an occultation optical depth profile to make very rough mass estimates. Indeed, both the Voyager PPS (Esposito *et al.* 1983b, hereafter referred to as EOW) and UVS (Holberg *et al.* 1982) teams performed such an analysis, with good agreement between their results.

As presented by EOW in their Eq. (4), the mass M_{12} between two ring radii R_1 and R_2 can be estimated by integrating the normal optical depth τ_n as a function of radius r, with a mean mass extinction coefficient $\bar{\kappa}$ obtained from model fits to density waves:

$$M_{12} = \frac{2\pi}{\bar{\kappa}} \int_{R_1}^{R_2} \tau_n(r) r \, dr. \tag{6}$$

Equation 6 assumes axisymmetry and a constant $\kappa(r)$. Because of the rings' differential rotation, axisymmetry is a good assumption. A constant κ is less valid: Showalter and Nicholson (1990) find a higher fraction of large particles in the A ring than in the C ring and inner Cassini Division, for example. Larger particles would present less cross-sectional area per unit mass, lowering κ locally. Further, $\kappa = \tau_n/\sigma$, where σ is the surface mass density. To date, the best indicators of surface mass density have been fits of linear models to sometimes-nonlinear spiral waves in the rings. Finding a meaningful representative optical depth inside a density wave is itself a nontrivial matter, since the sharp peaks of the waves are smoothed in the lower-resolution lightcurves (see Fig. 4). Using the 20- and 0.5-km PPS profiles, we were unable to reproduce the mean optical depth numbers stated for several density waves in EOW's Table I (EOW used the original 0.1-km-resolution profile). The mean optical depths of density waves in the 20- and 0.5-km PPS profiles also differed from each other, though mean optical depths in more quiescent regions were consistent. Finally, the high peak density of some of the waves may induce collision rates that locally alter the particle-size distribution, yielding a κ that is not representative of the rest of the rings.

Despite these many caveats, the optical depth integral remains the best mass estimate to date. Although the numbers produced may only approximate the actual mass, Eq. (6) is useful as an area-weighted means of comparing systematic differences between profiles, with or without $\bar{\kappa}$. As such it complements the mean optical depth of a ring section.

Only the optically deep B ring has thus far resisted this technique. The detection thresholds of EOW and Holberg *et al.* were $\tau_n = 2.55$ and $\tau_n = 2.85$, respectively, and Holberg *et al.* state that at least 15% of the B ring was below the limit. However, the Voyager observations provided many determinations of surface mass density from model fits to density and bending waves (EOW, Cuzzi *et al.* 1984), so all that was needed was an occultation with signal throughout the B ring. Because of the convolution

effects explained above under Optical Depth Profile Morphology, we did not attempt to derive surface mass densities by fitting models to density-wave trains, nor, for the reasons just discussed, were we able to determine useful mean optical depths inside the density waves (and thus potentially eliminate wavelength-dependent effects in our assumed $\bar{\kappa}$). We must thus use EOW's mass extinction coefficient of $(1.3 \pm 0.5) \times 10^{-2}$ cm^2/g to estimate ring masses from the IRTF 28 Sgr data. The estimated masses and the mean optical depths of each region from our egress profile are presented in Table III. Also included are the same quantities measured by the same method from the 20-km PPS profile used in Figs. 3 and 4, and, for convenient comparison, the numbers published in EOW. As one would expect from the similarities of the profiles, mass estimates from this occultation are similar to the Voyager numbers, with an overall tendency to estimate a slightly lower mass.

If the systematic large-scale differences between the IRTF 28 Sgr and PPS ring profiles do turn out to be due to indirect signal and extinction efficiency differences, then our geometric optical depths (i.e., optical depths related to the fraction of a beam occupied by the physical cross sections of particles in it) would all be greater than what we observed, and the optical-depth integrals and masses would thus increase. The mass of the B ring, in particular, would still be a lower bound.

CONCLUSIONS

The 28 Sgr event has produced a collection of data sets very rich both in potential science results and in analysis challenges. Work based on highly accurate optical depths in the ring system must likely await a correction for indirect signal and extinction efficiency. Such work would include more accurate optical-depth integrals and particle-size modeling of specific features based on multiple wavelengths of observation. Those aspects of the science that do not rely on accurate optical depths in the ring system, such as atmospheric work and pole fitting based on event times, can proceed with the existing profiles and are in fact being pursued by several groups [see French *et al.* (1993) and Hubbard *et al.* (1993) for pole solutions based on an ensemble of datasets, including this one].

These observations extend the wavelength coverage of the previously existing Saturn ring optical depth profiles into the infrared and provide a different chord from the Voyager occultations. Infrared imaging detectors, although still in their infancy, already offer much to the occultation observer. We have shown that, despite their complexity when compared to single-channel photometers, sufficient timing accuracy can be achieved with array systems to make them quite viable for occultations with much higher time resolution than this event required. Although considerably more analysis effort is re-

TABLE III
Ring Masses and Mean Optical Depths

Region	Inner edge[a] (km)	Outer edge[a] (km)	PPS[b] mean τ_n	$PPS_{20\,km}$ mean τ_n	IRTF mean τ_n	PPS[c] mass (10^{20} g)	$PPS_{20\,km}$ mass (10^{20} g)	IRTF mass (10^{20} g)
Inner C	74,809	83,859	0.08	0.08	0.12	2.8	2.9	4.2
Outer C	83,859	91,702	0.15	0.13	0.17	5.1	4.3	5.5
Inner B	91,702	100,148	1.21	1.01	0.96	45.5	39.8	36.8
Middle B	100,148	103,768	1.76	1.80	1.38	34.1	32.0	24.7
Outer B	103,768	117,643	1.84	1.86	1.68	113.8	137.7	122.9
Cassini	117,643	121,867	0.12	0.12	0.16	3.4	2.8	3.5
Inner A	121,867	130,313	0.70	0.56	0.48	39.8	28.6	24.3
Outer A	130,313	136,949	0.57	0.46	0.52	22.8	19.7	20.8
Total	74,809	136,949				284.5	267.8	242.7

Note. $\bar{\kappa} = (1.3 \pm 0.5) \times 10^{-2}$ cm^2/g. Formal fractional error of mass numbers derived in this work = ~0.4. Mass numbers presented in this table in most cases exceed their precision, but since the uncertainty is primarily in the constant mass extinction coefficient, the $PPS_{20\,km}$ and IRTF numbers can be compared. Since numbers from EOW were published with one digit of precision, they should not be compared to the others beyond one digit.

[a] As used by EOW, converted to km. 1 R_S = 60,330 km.

[b] As reported by EOW.

[c] Reported by EOW. Original publication had one digit of precision and used Saturn masses as a unit. Those numbers have been converted to grams with the planetary mass of 5.69×10^{29} g stated in EOW Table II.

quired with arrays than with single-channel photometers, the ability to model and subtract the background light field, and indeed to do so several times with different methods, can result in lightcurves with lower noise than would be possible with conventional aperture photometry. As larger, faster, quieter, and more linear chips become available, we hope that new cameras will be built with occultations in mind, and refer the prospective camera designer to our appendix on the topic.

APPENDIX: IMAGING OBSERVATIONS OF OCCULTATIONS

The use of charge-coupled devices (CCDs) and infrared arrays in several recent occultations (this work, Elliot *et al.* 1989, Dunham *et al.* 1989, French *et al.* 1989, di Cicco and Robinson 1989) represents a major step in the development of technology and techniques for occultations. This step is not an easy one; the amount of data to be handled, and its transmission rate, can be three orders of magnitude greater than for single-channel photometers. Accurate timing can be harder to achieve as well, because the instrument system through which the signal propagates is much more complex. With this many images (over 44,400 in our case), image processing must be automated, and there are many steps before one has a lightcurve. By contrast, the single-channel photometer observer leaves the observatory with a lightcurve in hand.

The advantages of imaging an occultation are quite definite, however. The most obvious is that photometry is done after the fact. Ordinary tracking errors (other than the failure of a major telescope component) do not exist, as the digital "aperture" can, if desired, be centered on the star in each image. One can try different combinations of apertures and models of the background light field. Also, the background to subtract from each raw data point is generally calculated from an image region a few arcseconds from the star on each frame, so a varying sky brightness is no longer a major problem. The result is a lightcurve with a significantly higher signal-to-noise ratio (SNR) than is generally possible with single-channel photometers. One can therefore observe fainter stars. In addition, having actual images makes it possible to inspect the data for the causes of anomalous lightcurve features.

A camera must be designed to observe occultations. The major new concerns are the amount of data, the data rate, the frame rate, and accurate absolute timing of images. The first three of these are interrelated, and a compromise in one can affect the others.

An 8-Hz occultation observed over 4 hr would produce over 10^5 images. If the detector is a 62×58-pixel infrared array producing 2-byte pixels, there will be 0.8 Gbytes of data to store. If multiple storage media (e.g., disks or tapes) are required to hold the data, the system must change between them without losing images. Many camera computers are real-time machines for which large or extra disks are either not available or are difficult to work into the configuration. One solution to this problem is to have the camera computer transmit the data over a network to a machine with a bigger disk. Under this scheme, no copy of the data is kept on the camera computer, so one must ensure that the end-to-end throughput is sufficient to handle the data rate of the array in its fastest readout mode. Many commercially available distributed filesystems do not meet this criterion, but it is a simple matter to write data transmission and reception programs that "shout" and "listen" on a network and that run effectively as fast as the hardware allows.

In the case of large arrays such as most CCDs, reading and recording the entire chip is both impractical and pointless: a relatively small subframe (50×50 pixels) can easily be made to contain the star and sufficient background for photometry. Reading more can take longer, reducing the time resolution possible. The camera software must therefore be programmed to do fast subframe readouts; in CCDs the uninteresting pixels are typically read as quickly as possible and discarded, and the region of interest is read at a slower rate to gain SNR from the readout amplifier. By adjusting the frame rate and the size of the stored frame, one has effective control over the amount of data to be saved. For the 28 Sgr event, our observing plan was a compromise to avoid saturating the detector (hence the $\frac{1}{12}$-sec integration times), oversample the lightcurve comfortably (4 frames/sec, achieved by averaging 3 frames of $\frac{1}{12}$ sec each), and not overflow the local storage (recording only 62×12-pixel subframes). Storage was on two disk drives, with no loss of data in the switch.

The final point to consider is timing. The main appeal of occultations is the high spatial resolution achievable by observing rapidly in time; time is the independent variable. The better one knows when each image was taken, the more accurate the lightcurve. In many occultations a timing error that would be unnoticed in more conventional observations can produce a very noticeable deviation in apparent position of the star behind the occulting object.

If observations from many stations are to be used simultaneously, their timing systems must have good synchronization to a common time base. In addition to the accuracy of the clock, one must also know the delay between a clock signal and the action of interest (shutter closing or array readout/clear). The timing accuracy required is determined by the event geometry and the nature of the object under study, but 0.1 msec is not an uncommon figure. The GOES system provides ~1 msec accuracy over a large region of the globe without the need to travel to a time standard for a sync to UT. Oven-stabilized quartz and rubidium oscillators, such as those used in this work, give sufficient accuracy to drive any system in use today (10^{-10} or better), but they require a sync and can be very sensitive to environmental conditions. The solution for occultation astronomers may lie in the Global Positioning System (GPS). GPS receivers are available commercially and are designed for field work. They can receive their satellite sync almost anywhere in the world, and run with accuracies similar to those of the quartz and rubidium standards.

Until recently, almost all observers based their timing on the introduction of an observable time signal from an accurate clock into their data stream. This can be done mechanically, for example by chopping with the secondary mirror; electrically, by adding a time signal to the analog output of a photometer; or digitally, by reading an external clock as an array reads out. Although these methods are adequate for most purposes, they require some effort during the analysis to recover the actual time of each frame. In this observation, we replaced the clock in the camera computer with an accurate one, and monitored it with a second clock. The timing solution of such a system is much simpler and the duration of each exposure is inherently more accurate.

Imaging occultations requires highly functional cameras that have been designed for the job. The additional design features are not expensive, but do require some thought and effort during development. The computer which runs a good occultation camera requires either sufficient storage capacity for a large number (10^5) of small images or the ability to transmit to another machine with such a storage medium. One must not lose data during media changes. In order to get sufficiently high time resolution and to save space, fast subframe readouts are important. Gaining this capability generally only requires writing software that takes advantage of the capabilities of the array. The most difficult feature to incorporate in an occultation camera is accurate timing. One needs a good clock, it needs a source of synchronization, and there must be a mechanism to associate its time with the data. In the ideal case, the accurate clock will be the clock running the camera, rather than an external reference. Although the cost of these enhancements is not negligible, one must also ask what the cost is of failing to achieve the best possible signal-to-noise ratio for an event, such as this

one, which is statistically likely to occur only once in 80 years (Elliot 1990).

ACKNOWLEDGMENTS

We thank M. D. Myers for the excellent occultation camera software, which allowed us to synchronize the images to an accurate time base. We also thank him for his care and diligence in counting microseconds in interrupt service routines and in transferring the occultation data from 78, 8-inch, 1-Mybte floppy disks to magnetic tape. We are grateful to T. Herbst for conceiving of and running the strip chart recorder mentioned under Timing System and for several other level-headed thoughts during the observation. We are indebted to N. Hironaka at the NIST WWVH station for loaning us the rubidium standard and for his help in analyzing the timing problems and recovering the absolute synchronization to UTC, R. L. Baron for designing the 60-Hz modification to the MIT portable clock, the staff of the IRTF for their considerable support of this observation, D. Mink and P. D. Nicholson for disseminating useful information on event circumstances prior to the occultation, P. D. Nicholson and R. G. French for their insightful comments and discussions during the data reduction phase, and referees B. Sicardy and M. Showalter for helpful suggestions. We thank N. M. Donahue for his vital assistance in creating the synthetic Saturn image. This work was supported in part by NSF Grant AST-8906011. IRAF is distributed by the National Optical Astronomy Observatories, which is operated by the Association of Universities for Research in Astronomy, Inc., under cooperative agreement with the National Science Foundation. The Astronomical Data Center at the NASA Goddard Space Flight Center provided infrared magnitudes.

REFERENCES

BARON, R. L. 1989. *Occultation Astronomy and Instrumentation: Studies of the Uranian Upper Atmosphere*. Ph.D. thesis, Massachusetts Institute of Technology.

BRAHIC, A., B. SICARDY, F. ROQUES, C. FERRARI, AND I. GRENIER 1989. Observation of the July 3, 1989 stellar occultation by Saturn and its rings. *Bull. Am. Astron. Soc.* **21,** 951.

CONNER, S. R. 1984. *Photometry of Hyperion*. Master's thesis, Massachusetts Institute of Technology.

CUZZI, J. N., AND J. A. BURNS 1988. Charged particle depletion surrounding Saturn's F ring: Evidence for a moonlet belt? *Icarus* **74,** 284-324.

CUZZI, J. N., J. J. LISSAUER, L. W. ESPOSITO, J. B. HOLBERG, E. A. MAROUF, G. L. TYLER, AND A. BOISCHOT 1984. Saturn's rings: Properties and processes. In *Planetary Rings* (R. Greenberg and A. Brahic, Eds.), pp. 73–199. Univ. of Arizona Press, Tucson.

DAVIS, L. 1987. Specifications for the Aperture Photometry Package. In *IRAF User Handbook,* Vol. 2b. National Optical Astronomy Observatories. P.O. Box 26732, Tucson, AZ 85726.

DI CICCO, D., AND L. J. ROBINSON 1989. Video images of the occultation of 28 Sagittarii by Saturn, July 2–3, 1989. *Bull. Am. Astron. Soc.* **21,** 953.

DUNHAM, E. W., J. L. ELLIOT, A. S. BOSH, L. L. CORDELLA, AND L. A. YOUNG 1989. KAO optical observations of the occultation of 28 Sgr by Saturn. *Bull. Am. Astron. Soc.* **21,** 932.

ELLIOT, J. L. 1990. An occult view of Titan. *Nature* **343,** 315–316.

ELLIOT, J. L., E. W. DUNHAM, A. S. BOSH, S. M. SLIVAN, L. A. YOUNG, L. H. WASSERMAN, R. L. MILLIS 1989. Pluto's atmosphere. *Icarus* **77,** 148–170.

ESPOSITO, L. W., M. O'CALLAGHAN, K. E. SIMMONS, C. W. HORD, R. A. WEST, A. L. LANE, R. B. POMPHREY, D. L. COFFEEN, AND M. SATO 1983a. Voyager photopolarimeter stellar occultation of Saturn's rings. *J. Geophys. Res.* **88,** 8643–8649.

ESPOSITO, L. W., M. O'CALLAGHAN, AND R. A. WEST 1983b. The structure of Saturn's rings: Implications from the Voyager stellar occultation. *Icarus* **56,** 439–452.

FORREST, W. J., J. L. PIPHER, Z. NINKOV, AND J. D. GARNETT 1989. InSb DRO array characteristics. In *Proceedings of the Third Infrared Detector Technology Workshop* (C. R. McCreight, Compiler), pp. 157–182. (NASA Tech. Mem. 102,209).

FRENCH, R. G., M. A. CLARK, E. TOLLESTRUP, E. ROBINSON, P. HARVEY, L. HEILMAN, R. FARR, AND R. STEINING 1989. The 3 July 1989 occultation of 28 Sgr by Saturn and its rings: Observations from McDonald Observatory. *Bull. Am. Astron. Soc.* **21,** 928.

FRENCH, R. G., P. D. NICHOLSON, M. L. COOKE, J. L. ELLIOT, K. MATTHEWS, O. PERKOVIĆ, E. TOLLESTRUP, P. HARVEY, N. J. CHANOVER, M. A. CLARK, E. W. DUNHAM, W. J. FORREST, J. HARRINGTON, J. L. PIPHER, A. BRAHIC, I. GRENIER, F. ROQUES, AND M. ARNDT 1993. Geometry of the Saturn system from the 3 July 1989 occultation of 28 Sgr and Voyager observations. *Icarus* **103,** 163–214.

HARRINGTON, J., E. W. DUNHAM, W. J. FORREST, AND J. L. PIPHER 1989. IRTF infrared imaging observations of the occultation of 28 Sgr by Saturn. *Bull. Am. Astron. Soc.* **21,** 954.

HOLBERG, J. B., W. T. FORRESTER, AND J. J. LISSAUER 1982. Identification of resonance features within the rings of Saturn. *Nature* **297,** 115–120.

HUBBARD, W., C. PORCO, D. HUNTEN, G. RIEKE, M. RIEKE, E. ASPHAUG, R. CLARK, V. HAEMMERLE, J. HALLER, J. HOLBERG, L. LEBOFSKY, R. MARCIALIS, D. MCCARTHY, B. MCLEOD, M. BUIE, J. ELIAS, D. JEWITT, E. PERSSON, T. BOROSON, S. WEST, R. LANDAU, AND W. SCHUSTER 1989. Preliminary results from the occultation of 28 Sgr by the Saturn system: Saturn. *Bull. Am. Astron. Soc.* **21,** 951.

HUBBARD, W. B., C. C. PORCO, D. M. HUNTEN, G. H. RIEKE, M. J. RIEKE, D. W. MCCARTHY, V. HAEMMERLE, R. CLARK, E. P. TURTLE, J. HALLER, B. MCLEOD, L. A. LEBOFSKY, R. MARCIALIS, J. B. HOLBERG, R. LANDAU, L. CARRASCO, J. ELIAS, M. W. BUIE, S. E. PERSSON, T. BOROSON, S. WEST, AND D. J. MINK 1993. The occultation of 28 Sgr by Saturn: Saturn pole position and astrometry. *Icarus* **103,** 215–234.

KILLIAN, A. M., AND A. S. DALTON 1985. Stellar occultations by Saturn's rings for 1985–1991. *Astron. J.* **90,** 2372–2376.

NEUGEBAUER, G., AND LEIGHTON 1969. Two-micron sky survey. In *Selected Astronomical Catalogs Volume 1* (CD-ROM released 1992). Astronomical Data Center, NASA Goddard Space Flight Center, Greenbelt, MD 20771.

NICHOLSON, P. D., M. L. COOKE, AND E. PELTON 1990. An absolute radius scale for Saturn's rings. *Astron. J.* **100,** 1339–1362.

NICHOLSON, P. D., O. PERKOVÍC, K. MATTHEWS, AND R. G. FRENCH 1991. Saturn's rings: optical depth profiles at $\lambda 3.9\ \mu m$ from the occultation of 28 Sgr. *Bull. Am. Astron. Soc.* **23,** 1178.

NULL, G. W., E. L. LAU, E. D. BILLER, AND J. D. ANDERSON 1981. Saturn gravity results obtained from Pioneer 11 tracking data and Earth-based Saturn satellite data. *Astron. J.* **86,** 456–468.

PORCO, C., W. HUBBARD, D. HUNTEN, G. RIEKE, M. RIEKE, E. ASPHAUG, R. CLARK, V. HAEMMERLE, J. HALLER, J. HOLBERG, L. LEBOFSKY, R. MARCIALIS, D. MCCARTHY, B. MCLEOD, M. BUIE, J. ELIAS, D. JEWITT, E. PERSSON, T. BOROSON, AND S. WEST 1989. Preliminary results from the occultation of 28 Sgr by the Saturn system: Rings. *Bull. Am. Astron. Soc.* **21,** 928.

REITSEMA, H., W. HUBBARD, D. HUNTEN, C. PORCO, N. BROSCH, Y. NEVO, E. CARREIRA, F. ROSSI, AND L. WASSERMAN 1989. Preliminary results from the occultation of 28 Sgr by the Saturn system: Titan. *Bull. Am. Astron. Soc.* **21,** 958.

SHOWALTER, M. R., AND P. D. NICHOLSON 1990. Saturn's rings through a microscope: Particle size constraints from the Voyager PPS scan. *Icarus* **87,** 285–306.

SICARDY, B., C. FERRARI, C. HUBERT, H. LECACHEUX, S. PAU, F. ROQUES, F. COLAS, F. SÈVRES, J. E. ARLOT, W. THUILLOT, J. L. VIDAL, C. BLANCO, S. CRISTALDI, C. BUILE, A. KLOTZ, AND E. THOUVENOT 1989. The occultation of 28 Sgr by Titan on July 3, 1989. *Bull. Am. Astron. Soc.* **21,** 958.

SINACHOPOULOS, D. 1989. A photometric study of wide visual double stars with significant relative proper motions. *Astron. Astrophys. Suppl. Ser.* **81,** 103–114.

TAYLOR, G. E. 1983. I.A.U. Commission 20 working group on the prediction of occultations by satellites and minor planets, Bulletin 30, 1983, Feb. 21.

TODY, D. 1986. The IRAF data reduction and analysis system. In *Instrumentation in Astronomy VI* (D. L. Crawford, Ed.) Proc. SPIE., Vol. 627, p. 733.